

Impact of the angular alignment on the crystal field and intrinsic doping of bilayer graphene/BN heterostructures

L. S. Farrar^{†,1}, G. Maffione^{†,1}, V.-H. Nguyen^{†,2}, K. Watanabe,³ T. Taniguchi,⁴ J.-Ch. Charlier,² D. Mailly,¹ and R. Ribeiro-Palau^{*1}

¹*Université Paris-Saclay, CNRS, Centre de Nanosciences et de Nanotechnologies (C2N), 91120 Palaiseau, France*

²*Institute of Condensed Matter and Nanosciences,*

Université catholique de Louvain (UCLouvain), 1348, Louvain-la-Neuve, Belgium

³*Research Center for Electronic and Optical Materials,*

National Institute for Materials Science, 1-1 Namiki, Tsukuba 305-0044, Japan

⁴*Research Center for Materials Nanoarchitectonics,*

National Institute for Materials Science, 1-1 Namiki, Tsukuba 305-0044, Japan

(Dated: October 3, 2024)

The energy gap of Bernal-stacked bilayer graphene can be tuned by applying a perpendicular electric field. The origin of this gap can be traced down to the breaking of its inversion symmetry by an onsite potential difference between the layers. This degree of tunability makes bilayer graphene a perfect playground for the study of the effects of electric fields, such as the crystalline field, which are developed when layers of other materials are deposited on top of it. Here, we introduce a novel device architecture allowing a simultaneous control over the applied displacement field and the crystalline alignment between two materials. Our experimental and numerical results confirm that the crystal field and electrostatic doping due to the interface reflect the 120° symmetry of the bilayer graphene/BN heterostructure and are highly affected by the commensurate state. These results provide an unique insight into the role of the twist angle in the development of internal crystal fields and intrinsic electrostatic doping in heterostructures. Our results highlight the importance of layer alignment, beyond the existence of a moiré superlattice, to understand and simulate the intrinsic properties of a van der Waals heterostructure.

Van der Waals heterostructures have become the perfect playground for condensed matter physics, specially since the angular alignment between layers was added as a new knob to tune their properties. Using the right combination of materials and twist angle, very complex phenomena can be observed in these heterostructures, such as, superconductivity [1–5], Mott insulators [6], anomalous quantum Hall effect [7], and more recently ferroelectricity [8–11]. However, mastering all the parameters to have an ultimate control of the properties of the heterostructure requires a deep understanding of the materials that compose the heterostructure and their interfaces. At these interfaces, crystal fields effects result from the electrochemical difference between layers, modifying the properties of the heterostructure [12]. Measuring the effect of the

crystal field in heterostructure has only been addressed recently for fixed crystallographic alignments [12]. This is mostly because investigating the angular variations will require the integration of dynamically rotatable van der Waals heterostructures [13, 14] with techniques that allow to control, both, top and bottom gates, which implies an important technological challenge.

In this work, we present a new device architecture that additionally to the rotational control of van der Waals heterostructures it also allows us to control both, top and bottom electrostatic gates. We demonstrate the performance of these new architectures using Bernal-stacked bilayer graphene (BBG) stacked between hexagonal boron nitride (BN). The control over both angular alignment and displacement field allows us to extract the angular dependence of the crystal electric field and intrinsic doping in a van der Waals heterostructure, pointing out the important role of layer alignment beyond the formation of moiré superlattices.

Figure 1a and b illustrate our novel device design, both as an overview (a) and its cross-section (b), Fig. 1c shows an atomic force microscope (AFM) image of a device in operation. The device comprises two main components: firstly, a Hall-bar shaped BBG on a BN layer, which itself sits atop a pre-etched graphite electrode, separated from the BBG by a BN layer; secondly, a rotator made of BN and Ti/Au, connected via an etched graphite electrode. The bottom graphite gate matches the rotator in diameter, and the graphite atop the rotator acts as a flexible van der Waals electrode for the application of a top gate voltage [15], creating a dual-gated region centered on the BBG Hall bar. The Si substrate is highly doped in order to improve the contact resistances on the BBG far from the rotator by tuning the carrier density with a gate voltage [16]. Full details of the fabrication procedures as well as optical images of the devices are provided in the Supplementary Note 1. It is important to mention that the bottom BN and graphene are intentionally misaligned, although at the moment of fabricating the devices we do not know the exact angular alignment.

The rotation procedure is identical to our previous re-

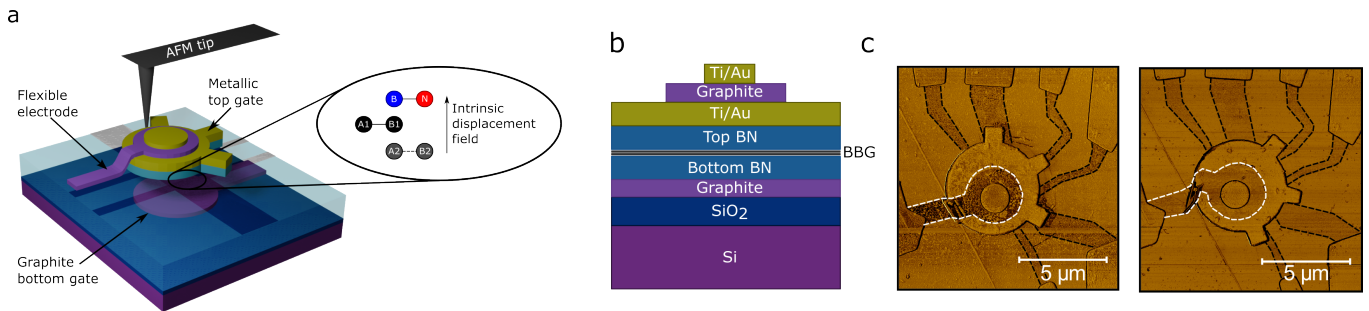


FIG. 1. **Dual gated rotatable device architecture.** **a** and **b**, Illustration of the new device architecture (a) and its schematic cross-section (b). The zoom in (a) is meant to signal the BBG unit cell and the intrinsic displacement field. A1(2) and B1(2) represent carbon atoms in sublattice A and B of layer 1 (2), respectively. B (blue) and N (red) represent boron and nitrogen atoms, respectively. **c**, Atomic force microscopy images (phase signal) of a complete device before and after rotation, the graphite flexible electrode (white dashed line) and graphene Hall bar (black dashed lines) have been highlighted for clarity.

ports [13, 17], wherein an AFM tip is used to mechanically push the rotator while measuring simultaneously the resistance of the sample, thus providing *in situ* control of the crystallographic alignment between the top BN and the BBG underneath. Overall the device allows for rotational control within 140° . In the AFM images of Fig. 1c we can see examples where the BN handle is rotated by about 37° after being pushed with the AFM tip. In this report we present results obtained mainly in three samples: Sample 1 and Sample 2, which share the same bottom BN, and Sample 3 (see Supplementary Note 2). The Hall bar widths w and lengths l are $w = l = 1.5 \mu\text{m}$. The carrier mobility of our samples ranged from 100,000 to 200,000 $\text{cm}^2\text{V}^{-1}\text{s}^{-1}$ for intermediate densities $\pm 0.65 \times 10^{12} \text{cm}^{-2}$ at $T < 40 \text{K}$. The mean free path was calculated to be $\approx 1.5 \mu\text{m}$ for the same carrier density below $T < 40 \text{K}$, reflecting the ballistic character of the charge transport for all of our devices.

To demonstrate the efficiency of our dual gated rotatable devices we show in Fig. 2a-c measurements of the four-probe resistance of sample 2 at 10 K as a function of V_{bg} and V_{tg} at three different angles: $\theta_{\text{top}} = 0^\circ$ (a), $\theta_{\text{top}} \approx 50^\circ$ (b) -where the moiré has little to no influence- and $\theta_{\text{top}} = 60^\circ$ (c).

In BBG, when the sign of V_{bg} and V_{tg} are opposite we observe a rapidly increasing $R_{4\text{P}}$ at the charge neutrality point (CNP). This maximum resistance for the three alignments, traces a straight line, with a slope determined by the ratio of the capacitive coupling of each layer $C_{\text{tg}}/C_{\text{bg}}$ which is in turn directly related to the thickness ratio between the top and bottom BN layers [18]. Along this diagonal line, the resistance strongly increases, a clear sign that a band energy gap is opening, as the magnitude of the displacement field $|D|$ increases [18–20]. The total displacement field, D , and total carrier density, n_{T} , of the system can be expressed as:

$$D = D_{\text{A}} - D_0 = \frac{e}{2\epsilon_0} [C_{\text{tg}}V_{\text{tg}} - C_{\text{bg}}V_{\text{bg}}] - D_0 \quad (1)$$

and

$$n_{\text{T}} = n - n_0 = [C_{\text{tg}}V_{\text{tg}} + C_{\text{bg}}V_{\text{bg}}] - n_0, \quad (2)$$

where D_{A} is the applied displacement field, D_0 is the residual or intrinsic displacement field of the sample, n_0 is the residual carrier density or intrinsic doping of the bilayer, $C_{\text{b(t)g}} = \epsilon_0\epsilon/d_{\text{b(t)}}e$ is the bottom (top) gate capacitive coupling, directly extracted from the Hall effect, ϵ is the BN dielectric constant, $d_{\text{b(t)}}$ is the BN thickness of the bottom (top) gate, and ϵ_0 is the vacuum permittivity.

The behavior of the two aligned positions $\theta_{\text{top}} = 0^\circ$ and $\theta_{\text{top}} = 60^\circ$, Fig. 2a and c, are dissimilar due to the 120° symmetry of the BN/BBG heterostructure [17] and are distinguished by the relative heights of the room temperature four-probe resistance measurements (see Supplementary Note 3 for further details). At low temperatures, their alignment is indicated by the presence of satellite peaks which appear symmetrically in carrier density around the CNP and occur due to the emergence of satellite Dirac points induced by scattering from the moiré superlattice potential [21]. The moiré wavelength λ is accurately determined by magneto-transport measurements and corresponds to $\lambda = 14.2 \pm 0.1 \text{nm}$ and $\lambda = 14.0 \pm 0.1 \text{nm}$ for the 0° and 60° alignments, respectively (see Supplementary Note 4 for further details).

Notice that, for the aligned positions Figs. 2a and c, contrary to the CNP, the resistance of the satellite peaks do not significantly change with displacement field, reflecting that these peaks are not affected by the breaking of inversion symmetry created by the displacement field.

To determine the residual or intrinsic displacement field, D_0 , we follow the resistance at the CNP as a function of both electrostatic gates. As explained before, the CNP can be clearly seeing as the red diagonal line in Fig. 2a-c, which indicate a strong resistance. The lowest value along this diagonal line position is the point where the applied V_{bg} and V_{tg} fully close the energy band gap. We have marked it by the crossing of white dashed lines in

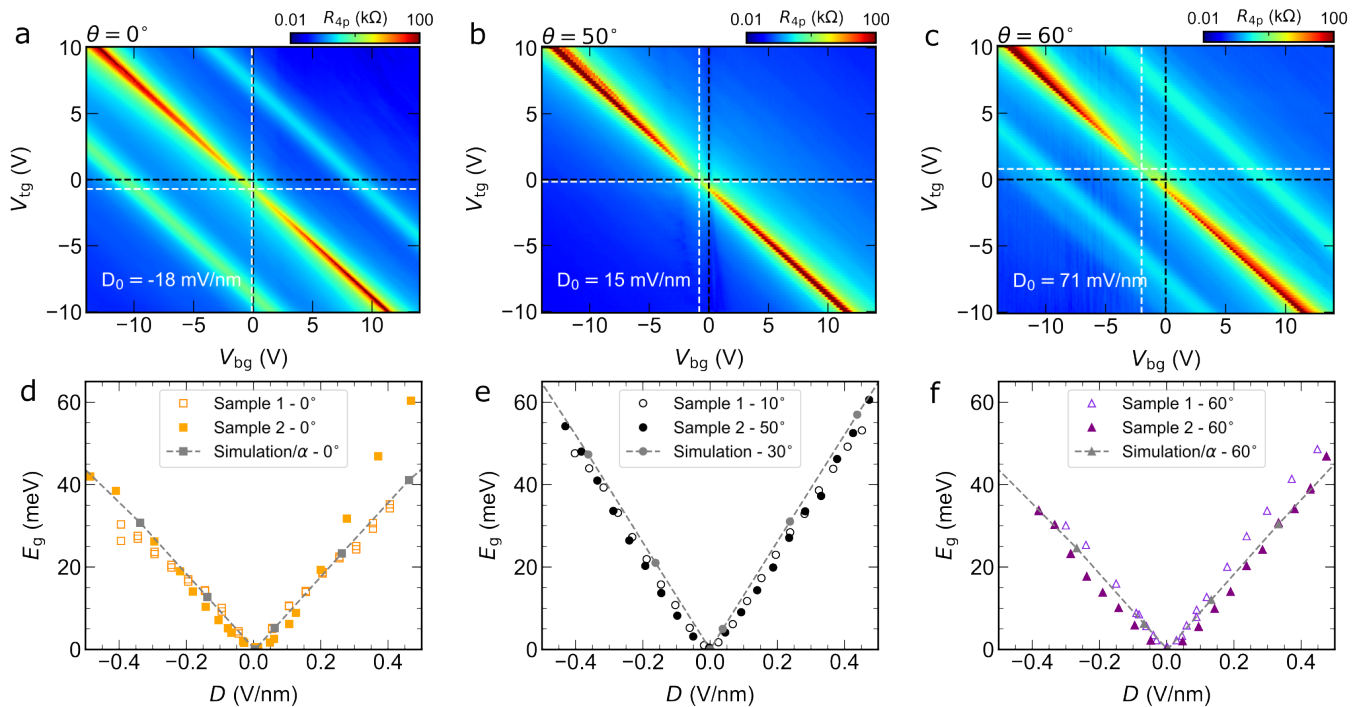


FIG. 2. **Dual gate effect at different rotational angles at $T = 10$ K.** Four-terminal resistance, R_{4P} , as a function of V_{tg} and V_{bg} at $\theta_{top} = 0^\circ$ **a**, $\theta_{top} = 50^\circ$ **b**, and $\theta_{top} = 60^\circ$ **c** of alignment between the top BN and the BBG for Sample 2. Black dashed lines represent the $V_{tg} = 0$ V and $V_{bg} = 0$ V lines. White dashed lines show the position of the lowest value on resistance of the CNP. **d-f**, Energy gap E_g as a function of the total displacement field, D , for three alignments: $\theta_{top} = 0^\circ$ **d**, $\theta_{top} = 10^\circ/50^\circ$ **e**, and $\theta_{top} = 60^\circ$ **f**, for Sample 1 and Sample 2. The data points are extracted from the Arrhenius plot in the thermally activated regime. Gray points with dashed lines are the result of numerical simulations divided by a factor $\alpha = 1.4$, see main text.

Figs.2a-c. At this point the applied displacement field, D_A , compensates the intrinsic displacement field, D_0 , of the sample. The origin of the intrinsic displacement field, as well as the residual doping, in single gated devices has been attributed to contaminants and residues on the surface of the device, however, it is more difficult to spot its origin in the case of double gated devices as ours, see discussion below.

The energy gap, E_g , induced by the applied displacement field can be determined via the temperature dependence of the CNP resistance. In the thermally activated regime, the resistance at the CNP decays exponentially as $R_{CNP} \propto \exp(E_g/(2k_B T))$, where k_B is the Boltzmann's constant and T the temperature. In Fig. 2d-f we plot the dependence of the energy gap with the total displacement field, D . All the curves follow an approximately linear dependence of the energy gap, as previously reported [18, 20, 22]. However, they do not have the same slope depending on the angular alignment. For the misaligned cases, Fig. 2e, the linear behavior is highly symmetric with respect to positive and negative displacement field, in agreement with previous reports [20]. On the other hand, for the aligned position, Figs. 2d and f the energy gap is smaller and slightly asymmetric with respect to

positive and negative displacement field. It is important to notice that, contrary to previous reports [22], and consistent with our earlier results [17], we do not observe any thermal activated behavior for the satellite peaks at any value of the displacement field.

Let's discuss these features. The energy band gap, E_g is given by [23, 24]

$$E_g = \frac{|\Delta|}{\sqrt{1 + (\Delta/\gamma_1)^2}}, \quad (3)$$

where γ_1 is the interlayer coupling strength between the graphene layers and Δ is the onsite potential difference expressed as [24, 25]:

$$\Delta = \frac{d_0 e \tilde{D}}{\epsilon_0 \epsilon_z} + \frac{d_0 e^2}{2\epsilon_0 \bar{\epsilon}} \delta n(\Delta). \quad (4)$$

The first term of Eq. 4 results from the external (applied or intrinsic) displacement field, where $\tilde{D}/\epsilon_0 = D$ is the total displacement field, d_0 is the interlayer spacing between the graphene layers, e is the elementary charge, and $\epsilon_z, \bar{\epsilon}$ are effective dielectric constants which vary depending on the model used [26, 27]. In our numerical

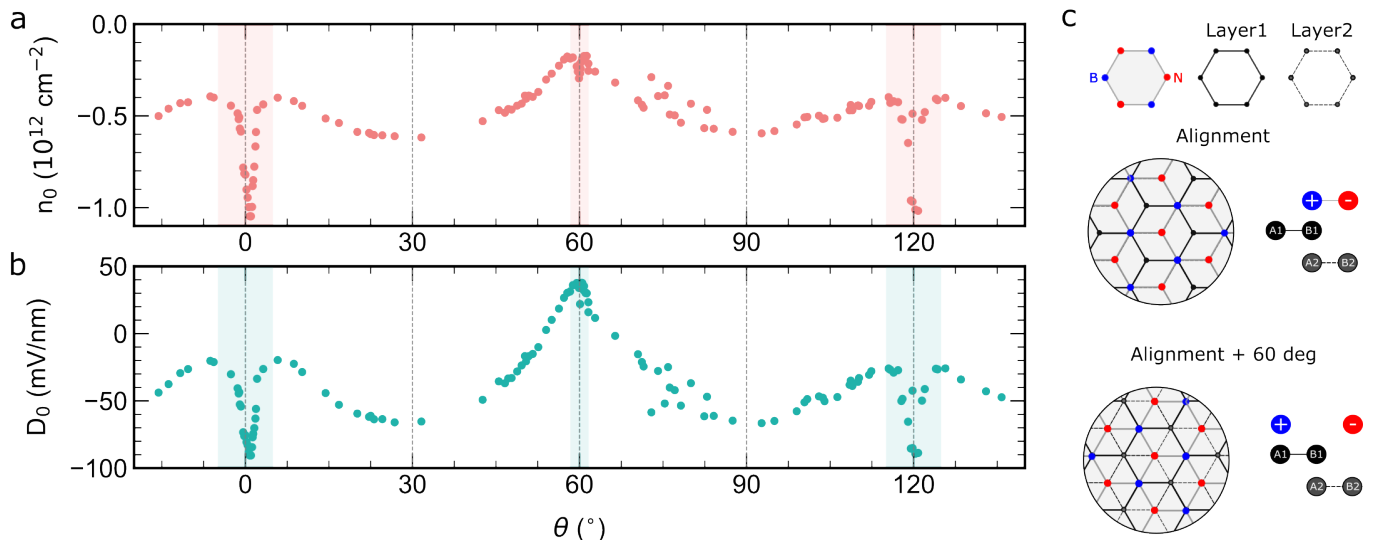


FIG. 3. **Intrinsic doping and crystal field as a function of angle.** **a**, Angular dependence of the intrinsic doping of the system. **b**, Angular dependence of the internal displacement field generated by the presence of the top and bottom BN. Shadow areas around 0° , 60° and 120° represent the $\pm 5^\circ$ ($\pm 2^\circ$) segment where a deviation from the expected behavior is observed for 0° (60°). Measurements taken for sample 3. **c**, Schematic representation of the two crystallographic alignments separated by 60° . Here positive charge accumulation on B (blue) atoms and negative charge accumulation on N (red) atoms is represented by (+) and (-) signs respectively.

simulation we use $\varepsilon_z = 2.5$ [26]. The second term of Eq. 4 results from the difference between the charge carrier densities in the upper n_1 and lower n_2 layers $\delta n = n_2 - n_1$. δn itself depends also on the value of Δ and as such requires a self-consistent solution which, for the misaligned case, is presented elsewhere [20, 26, 27].

Intuitively, the difference observed for the energy gap between the aligned and misaligned cases could be explained as an effect of the commensurate state near crystallographic alignment, a local enlargement of the graphene lattice constant to match that of BN whose lattice is 1.8% larger [17, 28]. However, we have performed numerical simulations (same numerical methods as in [17]) and the effects of the commensurate state in the energy gap seem only be relevant at larger displacement field (see Supplementary Note 5).

By directly comparing the result of our numerical simulations with the experimental results of the energy gap as a function of displacement field, Fig. 2d-f, we remark that the data from numerical simulations, for both aligned positions (0° and 60°), are off by a factor of $\alpha = 1.4$. The origin of this discrepancy might come from the second term of equation eq. 4 since the $\delta n(\Delta)$ parameter is not included in our numerical simulation given the complexity of its implementation in a large moiré cell. This term seem to be negligible at the misaligned position since our numerical simulations fit very well the experimental data.

We have extracted experimentally the angular dependence of δn , the difference between the charge carrier

densities in the upper and lower layers experimentally, Fig. 3a, by calculating the residual carrier density. For this, we performed resistance measurements around the CNP, by varying V_{bg} , for fixed values of V_{tg} to obtain the values of V_{tg} and V_{bg} for which the height of the CNP is the lowest, reflecting the closing of the energy gap. These experiments are performed at room temperature to have a large angular resolution. We have confirmed several points at low temperature to ensure their stability with temperature (for details see Supplementary Note 6). In Fig. 3a we can see that this intrinsic density, for misaligned angles, varies slowly with the angular alignment until it reaches the aligned positions. At these aligned positions, 0° and 60° , the behavior is opposite, increasing in magnitude for 0° and decreasing for 60° , this change is much more pronounced in the case of 0° .

We use the same measurements to extract D_0 . Fig. 3b shows the angular dependence of the intrinsic displacement field, which can be understood as the crystal field generated by the atomic configuration of the upper and bottom BN layers. In this measurements we recover the same general behavior as for the residual doping, a strong change at 0° occurring in a range of $\pm 5^\circ$ and a change in the opposite direction for 60° of alignment that saturates, in the case of the residual doping, for a range of angle of $\pm 2^\circ$.

In order to understand this non-trivial dependence we can start by comparing our experimental results with numerical simulations. As in the experiment, for the numerical simulations we have extracted the displacement field

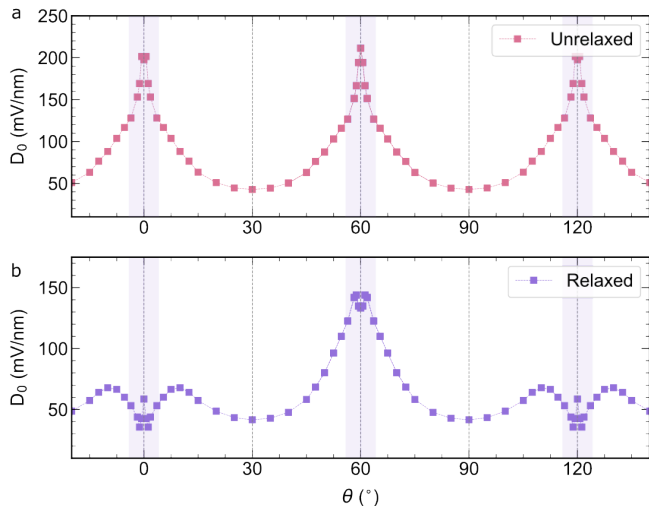


FIG. 4. **Crystal field numerical simulation.** Intrinsic displacement field as a function of the angular alignment between bilayer graphene and a BN layer for a system without atomic relaxation **a** and one where the atomic relaxation was taken into account **b**.

needed in order to close the energy gap of the electronic band structure for each angular alignment, from now we will refer to this as the crystal field, since it is a natural electric field generated by the atomic configuration of our system. We can start by discussing the unrelaxed case, Fig. 4a, for which we can see that the crystal field is minimum at 30° and 90° and increases strongly close to the aligned positions *e.i.*, 0° , 60° and 120° . Note that the minimum value of the displacement field is not zero because we have simulated a system with only one BN layer on top of the bilayer graphene. The strong increase of the crystal field at the aligned position is due to the combination of two factors: *i*) the electric field generated by the boron and nitrogen atoms by their proximity to the atoms A1 and B2 of the BBG (crystal field effect), see Fig. 3c, and *ii*) the moiré superlattice, which modifies the electronic band structure, even in the unrelaxed case. By using the numerical methods explained in [17] we relax the atomic structure, Fig. 4b. This atomic relaxation will give rise to the stretching of the graphene lattice inside the moiré cell and the formation of wrinkles of unstretched graphene around these cells.

For the relaxed numerical simulations near crystallographic alignment the crystal field is highly impacted by the moiré superlattice, as predicted in [29]. However, we can see that the impact for 0° and 60° has opposite behavior, which can be explained by looking at the unit cell of BBG for both aligned positions 0° and 60° , Fig. 3c. In the commensurate state, at the inner part of the moiré cell the BBG atoms are arranged in a BA stacking, between top layer of graphene and the BN layer. Here boron atoms are preferentially sitting on the carbon atoms, since this is the most energetically favorable

configuration [30]. We have demonstrated in our previous report [17] that the difference in the stacking for both alignment give rise to differences in the in plane atomic displacement and therefore to the electronic transport characteristics.

In the case of the crystal field, the difference between boron (+) and nitrogen (-) will generate a different charge accumulation between the sites A1 and B2, generating a different crystal field. This crystal field is expected to be stronger in one of the aligned cases because of the configuration of nitrogen and boron atoms, which also creates a larger $\delta n(\Delta)$. As this is observed within the same sample, we can disregard any effect of spurious doping, providing further evidence of the non-identical nature of the two moiré's in BBG/BN. It is important to note that our numerical simulations do not considered the bottom BN which we estimate induces an offset in Fig. 3a, explaining the asymmetry with respect to zero crystal field. This can be seen in the supplementary note 6 where the general behavior of the curve for a different sample is the same but there is an offset in the curve.

To conclude, we have developed a new device architecture that enables the rotation control of a van der Waals heterostructure while allowing for a simultaneous control of both bottom and top gates. We have used this device to reveal further details about effects of the moiré superlattice such as its impact on the evolution of the band gap by an external displacement field. We have measured for the first time the evolution of the atomic crystal field with angular alignment in a van der Waals heterostructure and revealed the strong effects of the commensurate state. The commensurate state in aligned bilayer graphene/BN structures is, as predicted by our numerical simulations, 120° periodic. These results highlight the importance of minding the layer alignment of each layer, beyond the existence of a moiré superlattice, to understand and simulate the intrinsic properties of a van der Waal heterostructure.

-
- [1] Yuan Cao, Valla Fatemi, Shiang Fang, Kenji Watanabe, Takashi Taniguchi, Efthimios Kaxiras, and Pablo Jarillo-Herrero. Unconventional superconductivity in magic-angle graphene superlattices. *Nature*, 556:43–50, April 2018.
 - [2] Hyunjin Kim, Youngjoon Choi, Cyprian Lewandowski, Alex Thomson, Yiran Zhang, Robert Polski, Kenji Watanabe, Takashi Taniguchi, Jason Alicea, and Stevan Nadj-Perge. Evidence for unconventional superconductivity in twisted trilayer graphene. *Nature*, 606:494–500, June 2022.
 - [3] Matthew Yankowitz, Shaowen Chen, Hryhoriy Polshyn, Yuxuan Zhang, K. Watanabe, T. Taniguchi, David Graf, Andrea F. Young, and Cory R. Dean. Tuning superconductivity in twisted bilayer graphene. *Science*, 363(6431):1059–1064, March 2019.

- [4] Yinjie Guo, Jordan Pack, Joshua Swann, Luke Holtzman, Matthew Cothrine, Kenji Watanabe, Takashi Taniguchi, David Mandrus, Katayun Barmak, James Hone, Andrew J. Millis, Abhay N. Pasupathy, and Cory R. Dean. Superconductivity in twisted bilayer WSe₂. *arXiv*, June 2024.
- [5] Yiyu Xia, Zhongdong Han, Kenji Watanabe, Takashi Taniguchi, Jie Shan, and Kin Fai Mak. Unconventional superconductivity in twisted bilayer WSe₂. *arXiv*, May 2024.
- [6] Guorui Chen, Lili Jiang, Shuang Wu, Bosai Lyu, Hongyuan Li, Bheema Lingam Chittari, Kenji Watanabe, Takashi Taniguchi, Zhiwen Shi, Jeil Jung, Yuanbo Zhang, and Feng Wang. Evidence of a gate-tunable Mott insulator in a trilayer graphene moiré superlattice. *Nat. Phys.*, 15:237–241, March 2019.
- [7] M. Serlin, C. L. Tschirhart, H. Polshyn, Y. Zhang, J. Zhu, K. Watanabe, T. Taniguchi, L. Balents, and A. F. Young. Intrinsic quantized anomalous Hall effect in a moiré heterostructure. *Science*, 367(6480):900–903, December 2019.
- [8] Zhiren Zheng, Qiong Ma, Zhen Bi, Sergio de La Barrera, Ming-Hao Liu, Nannan Mao, Yang Zhang, Natasha Kiper, Kenji Watanabe, Takashi Taniguchi, et al. Unconventional ferroelectricity in moiré heterostructures. *Nature*, 588(7836):71–76, 2020.
- [9] Ruirui Niu, Zhuoxian Li, Xiangyan Han, Zhuangzhuang Qu, Dongdong Ding, Zhiyu Wang, Qianling Liu, Tianyao Liu, Chunrui Han, Kenji Watanabe, et al. Giant ferroelectric polarization in a bilayer graphene heterostructure. *Nature Communications*, 13(1):6241, 2022.
- [10] Dahlia R Klein, Li-Qiao Xia, David MacNeill, Kenji Watanabe, Takashi Taniguchi, and Pablo Jarillo-Herrero. Electrical switching of a bistable moiré superconductor. *Nature nanotechnology*, 18(4):331–335, 2023.
- [11] Xiaodong Yan, Zhiren Zheng, Vinod K Sangwan, Justin H Qian, Xueqiao Wang, Stephanie E Liu, Kenji Watanabe, Takashi Taniguchi, Su-Yang Xu, Pablo Jarillo-Herrero, et al. Moiré synaptic transistor with room-temperature neuromorphic functionality. *Nature*, 624(7992):551–556, 2023.
- [12] Peter Rickhaus, Giulia Zheng, Jose L. Lado, Yongjin Lee, Annika Kurzmam, Marius Eich, Riccardo Pisoni, Chuyao Tong, Rebekka Garreis, Carolin Gold, Michele Masseroni, Takashi Taniguchi, Kenji Watanabe, Thomas Ihn, and Klaus Ensslin. Gap Opening in Twisted Double Bilayer Graphene by Crystal Fields. *Nano Lett.*, October 2019.
- [13] Rebeca Ribeiro-Palau, Changjian Zhang, Kenji Watanabe, Takashi Taniguchi, James Hone, and Cory R Dean. Twistable electronics with dynamically rotatable heterostructures. *Science*, 361(6403):690–693, 2018.
- [14] A. Inbar, J. Birkbeck, J. Xiao, T. Taniguchi, K. Watanabe, B. Yan, Y. Oreg, Ady Stern, E. Berg, and S. Ilani. The quantum twisting microscope. *Nature*, 614(7949):682–687, February 2023.
- [15] Evan J Telford, Avishai Benyamini, Daniel Rhodes, Da Wang, Younghun Jung, Amirali Zangiabadi, Kenji Watanabe, Takashi Taniguchi, Shuang Jia, Katayun Barmak, et al. Via method for lithography free contact and preservation of 2d materials. *Nano letters*, 18(2):1416–1420, 2018.
- [16] Rebeca Ribeiro-Palau, Shaowen Chen, Yihang Zeng, Kenji Watanabe, Takashi Taniguchi, James Hone, and Cory R Dean. High-quality electrostatically defined hall bars in monolayer graphene. *Nano letters*, 19(4):2583–2587, 2019.
- [17] Everton Arrighi, Viet-Hung Nguyen, Mario Di Luca, Gaia Maffione, Yuanzhuo Hong, Liam Farrar, Kenji Watanabe, Takashi Taniguchi, Dominique Maily, Jean-Christophe Charlier, et al. Non-identical moiré twins in bilayer graphene. *Nature Communications*, 14(1):8178, 2023.
- [18] Thiti Taychatanapat and Pablo Jarillo-Herrero. Electronic transport in dual-gated bilayer graphene at large displacement fields. *Physical review letters*, 105(16):166601, 2010.
- [19] Yuanbo Zhang, Tsung-Ta Tang, Caglar Girit, Zhao Hao, Michael C. Martin, Alex Zettl, Michael F. Crommie, Y. Ron Shen, and Feng Wang. Direct observation of a widely tunable bandgap in bilayer graphene. *Nature*, 459:820–823, June 2009.
- [20] Eike Icking, Luca Banszerus, Frederike Wörtche, Frank Volmer, Philipp Schmidt, Corinne Steiner, Stephan Engels, Jonas Hesselmann, Matthias Goldsche, Kenji Watanabe, et al. Transport spectroscopy of ultraclean tunable band gaps in bilayer graphene. *Advanced Electronic Materials*, 8(11):2200510, 2022.
- [21] Matthew Yankowitz, Jiamin Xue, Daniel Cormode, Javier D Sanchez-Yamagishi, K Watanabe, T Taniguchi, Pablo Jarillo-Herrero, Philippe Jacquod, and Brian J LeRoy. Emergence of superlattice dirac points in graphene on hexagonal boron nitride. *Nature physics*, 8(5):382–386, 2012.
- [22] Takuya Iwasaki, Yoshifumi Morita, Kenji Watanabe, and Takashi Taniguchi. Dual-gated hBN/bilayer-graphene superlattices and the transitions between the insulating phases at the charge neutrality point. *Phys. Rev. B*, 106(16):165134, October 2022.
- [23] Hongki Min, Bhagawan Sahu, Sanjay K Banerjee, and AH MacDonald. Ab initio theory of gate induced gaps in graphene bilayers. *Physical Review B*, 75(15):155115, 2007.
- [24] Edward McCann. Asymmetry gap in the electronic band structure of bilayer graphene. *Physical Review B*, 74(16):161403, 2006.
- [25] Jeil Jung and Allan H MacDonald. Accurate tight-binding models for the π bands of bilayer graphene. *Physical Review B*, 89(3):035405, 2014.
- [26] Sergey Slizovskiy, Aitor Garcia-Ruiz, Alexey I. Berdyugin, Na Xin, Takashi Taniguchi, Kenji Watanabe, Andre K. Geim, Neil D. Drummond, and Vladimir I. Fal’ko. Out-of-Plane Dielectric Susceptibility of Graphene in Twistrionic and Bernal Bilayers. *Nano Lett.*, July 2021.
- [27] Edward McCann and Mikito Koshino. The electronic properties of bilayer graphene. *Rep. Prog. Phys.*, 76(5):056503, April 2013.
- [28] CR Woods, Liam Britnell, Axel Eckmann, RS Ma, JC Lu, HM Guo, X Lin, GL Yu, Y Cao, Roman V Gorbachev, et al. Commensurate–incommensurate transition in graphene on hexagonal boron nitride. *Nature physics*, 10(6):451–456, 2014.
- [29] Nikita V. Tepliakov, QuanSheng Wu, and Oleg V. Yazyev. Crystal Field Effect and Electric Field Screening in Multilayer Graphene with and without Twist. *Nano Lett.*, May 2021.
- [30] Jeil Jung, Ashley M. DaSilva, Allan H. MacDonald, and Shaffique Adam. Origin of band gaps in graphene

on hexagonal boron nitride. *Nat. Commun.*, 6(1):1–11, February 2015.

- [31] B. Hunt, J. D. Sanchez-Yamagishi, A. F. Young, M. Yankowitz, B. J. LeRoy, K. Watanabe, T. Taniguchi, P. Moon, M. Koshino, P. Jarillo-Herrero, and R. C. Ashoori. Massive Dirac Fermions and Hofstadter Butterfly in a van der Waals Heterostructure. *Science*, May 2013.

ACKNOWLEDGEMENTS

The authors acknowledge discussions with Hervé Aubin Ulf Gennser, Nicolas Leconte and Cory Dean. This work was done within the C2N micro nanotechnologies platforms and partly supported by the RENATECH network and the General Council of Essonne. This work was supported by: ERC starting grant N° 853282 - TWISTRONICS (R.R.-P.), the DIM-SIRTEQ and DIM QuanTIP and IQUPS. R.R.-P. also acknowledge the Flag-Era JTC project TATTOOS (N° R.8010.19) and the Pathfinder project “FLATS” N° 101099139. V.H.N and J.-C.C. also acknowledge fundings from the Fédération Wallonie-Bruxelles through the ARC project “DREAMS” (N° 21/26-116), from the EOS project “CONNECT” (N° 40007563), and from the Belgium F.R.S.-FNRS through the research project (N° T.029.22F). Computational resources were provided by the CISM supercomputing facilities of UCLouvain and the CÉCI consortium funded by F.R.S.-FNRS of Belgium (N° 2.5020.11). K.W. and T.T. acknowledge support from the JSPS KAKENHI (Grant Numbers 21H05233 and 23H02052) and World Premier International Research Center Initiative (WPI), MEXT, Japan.

AUTHOR CONTRIBUTIONS STATEMENT

L.F, D.M. and R.R.-P. designed the experiment. L.F. and G.M. fabricated the devices for electron transport measurements and performed the electron transport experiments and analyzed the data. T.T. and K.W. grew the crystals of hexagonal boron nitride. V-H.N. and J.-Ch.C performed the numerical simulations. All authors participated to writing the paper. L.F., G.M. and V-H.N. contributed equally to this work.

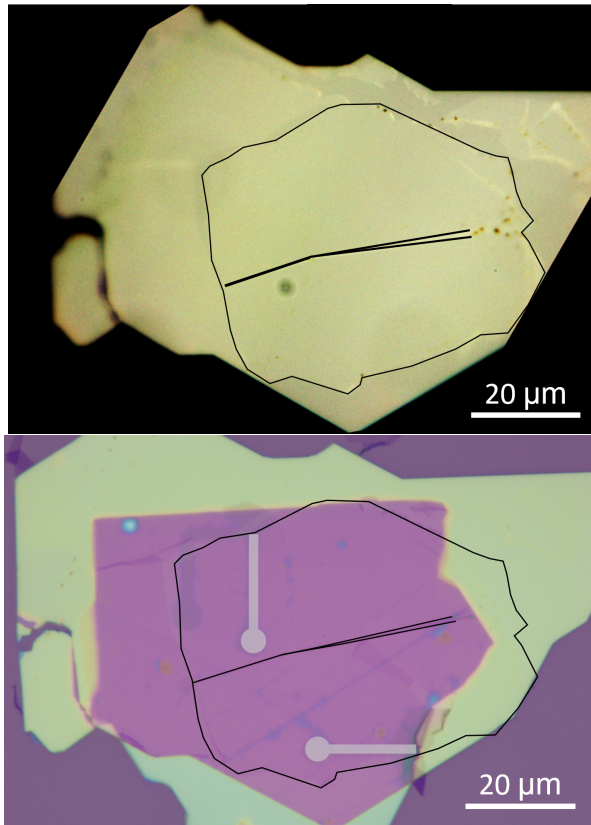
COMPETING INTEREST STATEMENT

The authors declare no competing interests.

SUPPLEMENTARY INFORMATION

SUPPLEMENTARY NOTE 1: DEVICE FABRICATION

To fabricate our samples, we start by building a heterostructure with conventional dry stacking methods. First an hexagonal boron nitride (BN) flake is picked up using a polymer film (PPC) and is then used to pick up a flake of graphite; the structure is flipped and deposited on a clean substrate. We can proceed by patterning the graphite for the local gates using electron beam lithography followed by oxygen plasma etching.

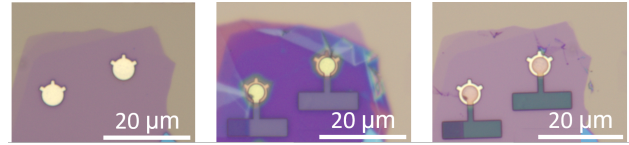


Supplementary Figure 1. **Optical images taken during the fabrication process.** (Top), BN and BBG on the polymer film used for dry-transfer, the graphene flake is highlighted by a black contour. (Bottom), final stack, local gates are colored in white and graphene flake is drawn to highlight the position of the samples.

Another BN flake, the bottom BN flake of the device, is picked up using PPC, and with this a bilayer graphene flake, this stack is flipped and deposited onto the previously fabricated graphite back gate. Lithography and oxygen plasma etching are now used to pattern the Hall bar shape.

Top gates are fabricated separately: rotators, which

we call handles, are made of BN covered with a thin layer of titanium (≈ 10 nm), used to improve adhesion, and a layer of gold (≈ 100 nm). The metal is deposited after patterning the rotator shape on the flake with e-beam lithography. After lift-off we use the deposited metal as a mask and etch the uncovered BN with CHF_3 plasma (Fig. 2a). To fabricate the flexible graphite electrode which completes our top gates we deposit a graphite flake on the BN-gold handle (Fig. 2b) and etch the desired shape using e-beam lithography and O_2 plasma (Fig. 2c).

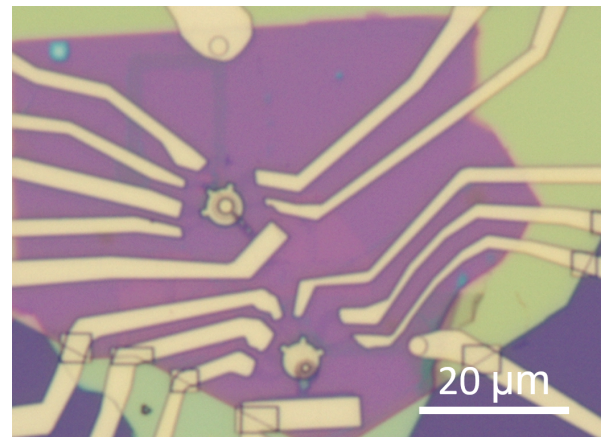


Supplementary Figure 2. **Steps in the top gate fabrication .** a, Handles made of BN covered with titanium and gold. b, Flake of graphite deposited on the handles. c, Graphite etched in the shape of a flexible electrode.

Once the top gates and flexible electrodes are ready, they are carefully transferred on the samples making sure to match the center of the handle with the center of the Hall bar.

After the transfer of the top gate and flexible electrode, the electrical connections were defined using e-beam lithography followed by deposition of 10 nm Ti and 100 nm Au. If required, a 1D electrical contact is made to the back-gate by CHF_3 plasma etching. Additionally, small (1-2 μm diameter) Ti/Au discs were also deposited onto the graphite of the top-gate to improve the positioning of the graphite flexible electrode after rotation, if needed.

An optical microscope image of a final device can be seen in Fig. 3.



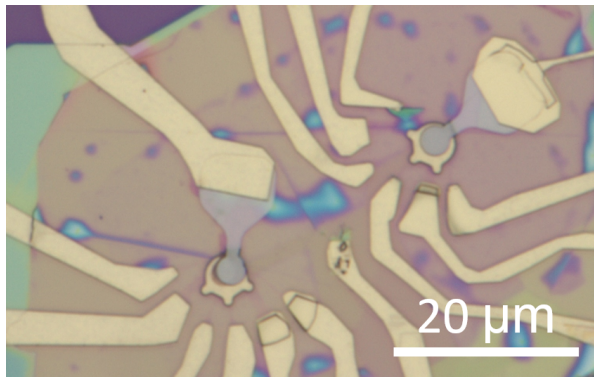
Supplementary Figure 3. **Final device for samples 1 and 2.** Optical image of the final device where samples 1 and 2 can be seen.

SUPPLEMENTARY NOTE 2: SAMPLES DESCRIPTION

Sample 1 and Sample 2 (LSFTG2B): These samples share the same bottom BN and they both have independent local graphite bottom gates. Hall bar widths w and lengths l are $w = l = 1.5 \mu\text{m}$. Thickness of the bottom BN is 70 nm (capacitive coupling of $C_{\text{bg}} = 2.64 \times 10^{15} \text{ V}^{-1}\text{m}^{-2}$), the top BN of Sample 1 is 73 nm thick with $C_{\text{tg1}} = 2.21 \times 10^{15} \text{ V}^{-1}\text{m}^{-2}$ and for Sample 2 it is 50 nm thick with $C_{\text{tg2}} = 3.2 \times 10^{15} \text{ V}^{-1}\text{m}^{-2}$. Capacitive coupling values are obtained from Hall measurements.

Although the two samples share the bottom BN, the alignment between the latter and BBG is not identical. During fabrication of the stack the flake of bilayer graphene tore thus producing a fold (as shown in Fig. 1); from optical images we can estimate the fold to have produced a $\approx 5^\circ$ rotation between the two areas of the flake. The devices were then fabricated on opposite sides with respect to this fold, leading to different angles between BBG and the bottom BN.

Sample 3 (LSFTG3B): this sample has a local graphite back gate, bottom BN thickness is 44 nm and $C_{\text{bg}} = 2.76 \times 10^{15} \text{ V}^{-1}\text{m}^{-2}$, top BN is 70 nm thick with $C_{\text{tg}} = 4.29 \times 10^{15} \text{ V}^{-1}\text{m}^{-2}$, both values are calculated by geometrical capacitance. Hall bar widths w and lengths l are $w = l = 1.5 \mu\text{m}$, an optical image of the sample can be seen in Fig. 4.



Supplementary Figure 4. **Optical image Sample 3.** The measured sample is the one on the [left/right](#), the other sample showed open electrical contacts.

SUPPLEMENTARY NOTE 3: ANGULAR CONTROL

Using an identical rotation procedure to previous work [13, 17], we are able to deterministically vary the angle of alignment between the BBG and the BN rotator, which also acts as a top-gate. Briefly, using an atomic force

microscope (AFM) and the feedback loop turned off we are able to apply, in contact mode, a lateral force to the handle with the AFM tip in order to move it. The trajectory for the AFM tip was then defined such that the tip comes into contact with one of the arms of the rotator. Due to friction between the BN rotator and the surface below, the arm acts as a lever, translating the linear motion of the tip into an angular motion.

To determine the relative alignment of the BN/BBG, *in situ* charge transport measurements were performed at room temperature. During rotation of the top-gate, the back gate is fixed at a voltage corresponding to a carrier density $n \sim 0.5\text{-}1 \times 10^{12} \text{ cm}^{-2}$. At room temperature, due to the effects of thermal broadening, the CNP and satellite peak of BBG are merged[17], however, as the BN approaches alignment with the BBG below, the resistance within this carrier density regime increases with alignment due to the emergence of the satellite peak, reaching a maximum at 0° and 60° of alignment between the BBG and BN.

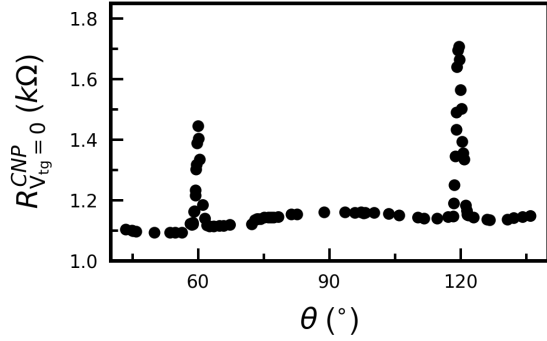
Upon cooling to 1.5 K, the CNP and satellite peaks become distinguishable from each other and the alignment angle can be estimated using the formula $n_{\text{sat}} = C_g(V_g - V_{\text{CNP}})$ where C_g is the capacitive coupling of one of the two gates, V_g is the applied voltage, V_{CNP} is the position in voltage of the CNP, and n_{sat} is the carrier density at which the satellite peak is observed, the full filling of the moiré miniband.

The angle of alignment is then calculated from the formula $n = 8/\sqrt{3}\lambda^2 = 8\sqrt{2}(1 + \delta)(1 - \cos\theta) + \delta^2/(\sqrt{3}[1 + \delta]a)$, where λ is the moiré wavelength, a is the lattice constant of graphene, δ is the lattice mismatch between BN and graphene, and θ is the rotational mismatch between the layers [21].

Identifying 0° and 60° of alignment

As described in the main text and in our previous reports [17], as the rotator gets close to its crystallographic alignment with graphene, the resistance peak at charge neutrality becomes higher; this enlargement occurs every 60° because of crystallographic alignment but, as previously reported, it is 120° periodic since 0° and 60° aligned positions are not equivalent.

In Fig. 5 we show the difference in the height of CNP between two alignments covering $> 60^\circ$ rotation. This allows us to identify the highest resistance peak, which we label as 0° aligned position coherently with our previous report[17]. The angles reported in the x axis correspond to the ones reported in figure 3 of the main text, with the equivalence of $0^\circ = 120^\circ$.



Supplementary Figure 5. **Identification of alignment.** Resistance value of the CNP as a function of the angular alignment, measured without applied top gate voltage with the AFM at room temperature, in the range from 40° to 140° .

SUPPLEMENTARY NOTE 4: BROWN-ZAK OSCILLATIONS

To precisely measure the moiré length in aligned positions, we perform magneto transport measurements and plot the longitudinal conductivity, σ_{xx} , as a function of the moiré filling, n/n_0 , and magnetic field, B , Fig. 6. In these plots we can see the appearance of horizontal lines when the central and satellite fans intercept.

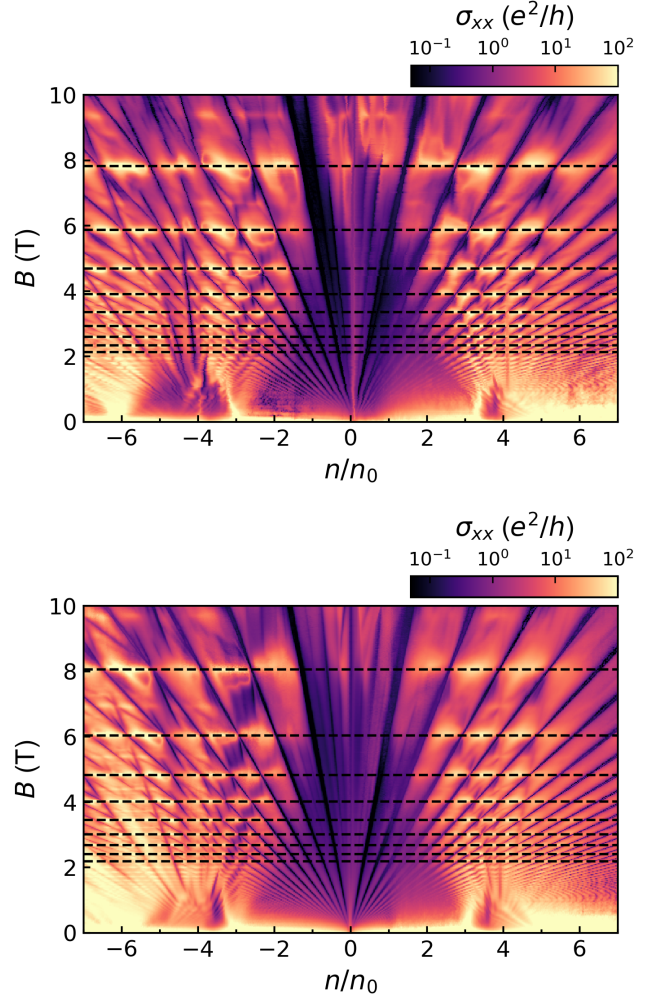
This correspond to the magnetic field, B , at which one flux quantum threads the superlattice moiré unit cell area, $\phi = B3\sqrt{3}\lambda^2/2$ is an integer fraction of the magnetic flux quantum ϕ_0 .

For the alignments reported in the main text for Sample 1, 0° corresponds to a moiré wavelength $\lambda = 14.25 \pm 0.1$ nm and 60° with $\lambda = 14.0 \pm 0.1$ nm.

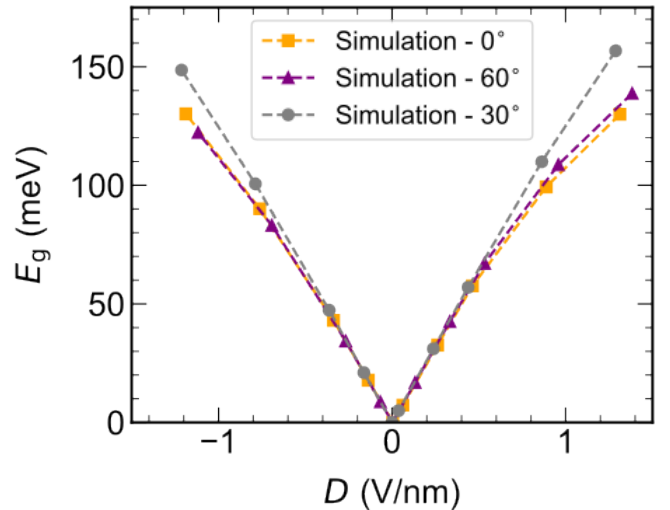
It is important to remark that this is a purely geometrical effect and gives therefore a very accurate estimation of the moiré superlattice size without referencing electrostatic parameters [31].

SUPPLEMENTARY NOTE 5: NUMERICAL SIMULATION

The commensurate state in aligned graphene/BN structures induces a variation in the interlayer coupling strength γ_1 , interlayer spacing and a re-normalisation of the effective mass. Furthermore, the two non-identical alignments lead to different levels of atomic displacement (*i.e.* strain), which in turn leads to differences in the predicted band structures through variation of the effective mass of the low energy bands near the CNP [17].



Supplementary Figure 6. **Brown-Zak oscillations.** Magneto-transport measurements for Sample 1 at 0° aligned position (top) and 60° aligned position (bottom).



Supplementary Figure 7. **Energy gap numerical simulations.**

SUPPLEMENTARY NOTE 6: INTRINSIC DISPLACEMENT FIELD MEASUREMENTS

In order to extract the crystal field we performed four probe measurements as a function of both (bottom and top) gates inside our AFM as we change the angular

alignment. An example of these measurements can be seen in Fig. 8. Using these measurements we extract the position of the minimum value of the CNP for the top and bottom gates and use this to calculate the intrinsic displacement field and doping, Fig. 9.

